ated by applying voltage pulses on each side of the Co cluster is shown in Fig. 3B. Spectroscopic data recorded above the Co site (Fig. 3C) exhibit an average level spacing, indicated by gray arrows, of ~0.15 eV. This spacing agrees with expectations (*3, 29*), $\Delta E \sim 1.67\ \mathrm{eV}/L$ (= 11 nm), and notably is an order of magnitude larger than the width of the Kondo resonance. The spectroscopic results recorded at the same position as the Co site are substantially different from the overall *dI*/*dV* structure observed in previous experiments on shortened metallic SWNTs (*3*): the peak amplitude at E_F appears markedly enhanced relative to the other energy-level peaks.

To investigate the origin of this increased conductance, we characterized the level structure near E_F versus distance from the cluster (Fig. 3D). Interestingly, the amplitude of this central peak at E_F decreases over the same length scale, 2 nm, as the Kondo resonance decays from a Co cluster along an extended 1D SWNT, although the amplitude of peaks at $E \neq E_F$ is similar. The enhanced conductance at E_F provides evidence to how sensitive the electronic properties of metallic nanotubes are to magnetic impurities, even in finite-sized structures. Finally, it has been predicted that in confined electron systems where $\Delta E > T_K$, the Kondo resonance will be split into a series of subpeaks spaced by ΔE and will exhibit different features around E_F, depending on whether the total number of electrons in the box is odd or even (*28*). Within this framework, we can tentatively assign our finite-sized magnetic structure as an odd Kondo box, because a peak rather than a dip is observed at E_F. Studies using gated tips (*30*) could probe this assignment further by changing the number of electrons on the nanotube quantum box.

Overall, the present study indicates that many basic features of the Kondo effect are similar in 1D strongly interacting systems as they are in Fermi liquids. SWNT hosts of varying size provide much flexibility for investigating the Kondo effect at different energy scales. When this is combined with investigations of temperature and magnetic field, it could add much to our understanding of the Kondo resonance and how electron correlations in 1D modify the standard picture. We believe that STM will be critical to such studies, and moreover, may uncover unique applications of these nanostructures.

References and Notes

1. R. Saito, G. Dresselhaus, M. S. Dresselhaus, *Physical Properties of Carbon Nanotubes* (Imperial College Press, London, 1998).
2. C. Dekker, *Phys. Today* **52** (no. 2), 22 (1999).
3. T. W. Odom, J.-L. Huang, P. Kim, C. M. Lieber, *J. Phys. Chem B* **104**, 2794 (2000).
4. J. W. G. Wildoer, L. C. Venema, A. G. Rinzler, R. E. Smalley, C. Dekker, *Nature* **391**, 59 (1998).
5. T. W. Odom, J.-L. Huang, P. Kim, C. M. Lieber, *Nature* **391**, 62 (1998).
6. P. Kim, T. W. Odom, J.-L. Huang, C. M. Lieber, *Phys. Rev. Lett.* **82**, 1225 (1999).
7. S. J. Tans *et al.*, *Nature* **386**, 474 (1997).
8. M. Bockrath *et al.*, *Science* **275**, 1922 (1997).
9. S. J. Tans, R. M. Verschueren, C. Dekker, *Nature* **393**, 49 (1998).
10. R. Martel, T. Schmidt, H. R. Shea, T. Hertel, Ph. Avouris, *Appl. Phys. Lett.* **73**, 2447 (1998).
11. M. Bockrath *et al.*, *Nature* **397**, 598 (1999).
12. Z. Yao, H. W. C. Postma, L. Balents, C. Dekker, *Nature*, **402**, 273 (1999).
13. J. Kondo, *Prog. Theor. Phys.* **32**, 37 (1964).
14. L. Grigorian *et al.*, *Phys. Rev. B* **60**, R11309 (1999).
15. J. Li, W.-D. Schneider, R. Berndt, B. Delley, *Phys. Rev. Lett.* **80**, 2893 (1998).
16. V. Madhavan, W. Chen, T. Jamneala, M. F. Crommie, N. S. Wingreen, *Science* **280**, 567 (1998).
17. H. C. Manoharan, C. P. Lutz, D. W. Eigler, *Nature* **403**, 512 (2000).
18. A. Schiller, S. Hershfield, *Phys. Rev. B* **61**, 9036 (2000).
19. The Co clusters were produced in ultrahigh vacuum by resistively heating Co wire wrapped around a W filament with the sample held at ~100 K. The sample consisted of laser-ablated SWNTs supported on Au(111)/mica surfaces, prepared as in (*3*).
20. Average cluster sizes were less than 2 nm in width, and were typically 0.5 to 1 nm in diameter, containing about 3 to 30 atoms, respectively. Because atom diffusion along the sample surface leads to cluster formation, we estimate that a majority of the smaller clusters exhibit single- or double-atom heights.
21. T. W. Odom, J.-L. Huang, C.-L. Cheung, C. M. Lieber, data not shown.
22. P. W. Anderson, *Phys. Rev.* **124**, 41 (1961).
23. A. C. Hewson, *The Kondo Problem to Heavy Fermions* (Cambridge Univ. Press, Cambridge, 1993).
24. U. Fano, *Phys. Rev.* **124**, 1866 (1961).
25. The Fano model assumes a single spin-½ atom within a free-electron host. The Co/SWNT system is more complicated than this for several reasons and deserves further theoretical treatment. First, the net spin in the clusters and the details of their ferromagnetic exchange coupling are unknown. Second, the precise nature of Co clusters coupling to the nanotube surface is not well defined. Finally, electron-electron correlations of the nanotube host may be important.
26. We find that small clusters with diameters between 0.5 to 0.8 nm (about 3 to 10 atoms) exhibit a Kondo resonance peak, while larger clusters with diameters >1 nm (>30 atoms) do not, and instead exhibit an energy-level spectrum characteristic of small Co nanoparticles, similar to spectra observed in transport measurements by S. Gueron *et al.* [*Phys. Rev. Lett.* **83**, 4148 (1999)].
27. D. M. Duffy, J. A. Blackman, *Phys. Rev. B* **58**, 7443 (1998).
28. B. Wolfgang, J. K. Thimm, J. von Delft, *Phys. Rev. Lett.* **82**, 2143 (1999).
29. L. C. Venema *et al.*, *Science* **283**, 52 (1999).
30. L. Gurevich, L. Canali, L. P. Kouwenhoven, *Appl. Phys. Lett.* **76**, 384 (2000).

31. We thank P. Brouwer, B. Halperin, T. Oosterkamp, and Y. Oreg for helpful and stimulating discussions. C.M.L. acknowledges support of this work by the NSF.

18 August 2000; accepted 3 October 2000

Modulated Chemical Doping of Individual Carbon Nanotubes

Chongwu Zhou, Jing Kong, Erhan Yenilmez, Hongjie Dai*

Modulation doping of a semiconducting single-walled carbon nanotube along its length leads to an intramolecular wire electronic device. The nanotube is doped *n*-type for half of its length and *p*-type for the other half. Electrostatic gating can tune the system into *p*-*n* junctions, causing it to exhibit rectifying characteristics or negative differential conductance. The system can also be tuned into *n*-type, exhibiting single-electron charging and negative differential conductance at low temperatures. The low-temperature behavior is manifested by a quantum dot formed by chemical inhomogeneity along the tube.

Energy-band engineering by doping has played a critical role in microelectronics. Rectifying *p*-*n* junctions, bipolar junctions, and field-effect transistors (*1*) have been important electronic components based on doped bulk semiconductors. Negative differential conductance, discovered by Esaki in degenerately doped *p*-*n* junctions (*2*), has found wide applications for high-frequency amplifiers and oscillators. Carbon nanotubes are a new class of material potentially useful as key elements for future miniaturized electronics (*3*). Similar to ideas in conventional materials, designed doping of nanotubes is expected to yield nanoscale devices with interesting properties and functions (*4*–*6*). We report modulated chemical doping of individual single-walled carbon nanotubes (SWNTs) along their lengths for intrawire devices (*6*–*9*) including gate-tunable nanotube *p*-*n* junctions and Esaki diodes. These on-tube devices have been proposed by theory recently (*4, 5*). It is also found that at low temperatures, small inhomogeneity in the doping profile manifests strongly in the quantum transport behavior of nanotubes.

Modulated chemical doping is performed with two terminal devices of individual SWNTs grown on catalytically patterned SiO_2 surface (Fig. 1) (*10*). The SWNT employed in the doping experiment has a diameter of ~2 nm and a length of 3.5 μm between the source (S) and drain (D) metal electrodes (Fig. 1B). A 340-nm-thick polymethylmethacrylate (PMMA) layer covers the left half of the nanotube, leaving the right half exposed (Fig. 1A). Prior to doping, the

Department of Chemistry, Stanford University, Stanford, CA 94305, USA.

*To whom correspondence should be addressed. E-mail: hdai@chem.stanford.edu

SWNT behaves as a *p*-type semiconductor, as manifested by drastically reduced conductance under increasing positive gate-voltages (*11–13*). Several groups have consistently observed *p*-type doping of SWNTs and have attributed it to adsorbed molecules, chemical groups on substrates, or charge transfer with metal electrodes (*11–15*). The predicted band gap for the 2-nm-diameter semiconducting SWNT is $E_g \sim 0.35$ V. Potassium doping of the SWNT is carried out in vacuum by electrical heating of a potassium source while monitoring the conductance of the sample (*16*). The PMMA-covered half of the SWNT remains *p*-type. Potassium atoms adsorb onto the surface of the uncovered part of the SWNT, donating electrons to convert the nanotube segment from *p*- to *n*-type. Potassium doping of individual SWNTs along their entire length has been carried out previously (*16–18*). The importance of controlling the doping profile on a single nanotube has been suggested by experimental work (*6*), but so far, only accidental doping of part of a tube has been reported (*6*).

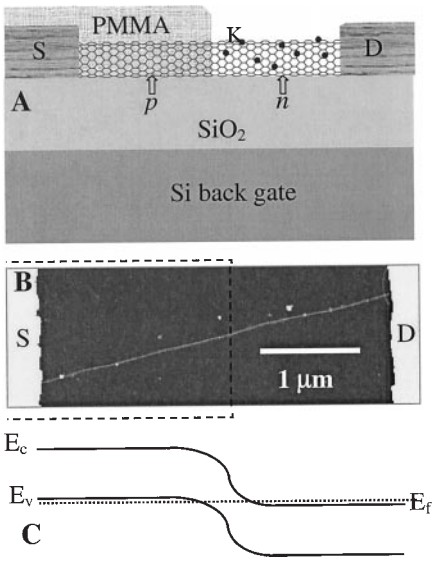

Fig. 1. An SWNT with modulated chemical doping. (**A**) Device scheme with the SWNT contacted by two Ni/Au electrodes. The Si substrate is used as a back-gate. The SiO_2 layer is 500 nm thick. The right half of the SWNT is doped by evaporating K atoms (black dots) from an alkaline metal dispenser (SAES Getters USA, Colorado Springs, CO) in an evacuated (10^{-6} torr) insert designed for variable-temperature electrical measurements. This approach allows low-temperature measurements of the doped sample with the insert placed into a helium dewar without breaking vacuum. Doping conditions: current passed through the potassium source for resistive heating is 4.5 A and the time duration for the doping is 2 hours. During doping, the conductance of the sample initially decreases and then recovers. Detailed doping setup and conditions can be found in (*16*). (**B**) Atomic force microscopy image of the SWNT recorded before PMMA coating of the left half and doping. The bright regions at the two ends are the electrodes. Dashed lines are drawn to highlight the later PMMA-covered region. (**C**) A band diagram for the system. E_c, E_f, and E_v represent the conduction band, Fermi level, and valence band, respectively.

The current versus back-gate-voltage (I-V_g) characteristics of the sample recorded at room temperature exhibits interesting features (Fig. 2A). Note that the drain electrode (Fig. 1A) was grounded in all of the measurements. The conductance for V_g between -20 and -12 V (regime I) is near zero. A hump with substantial conductance is notably present as V_g increases to $-12\ \text{V} < V_g < -7$ V (regime II). The conductance becomes suppressed again for V_g between -7 and -1 V (regime III), after which the conductance increases in a near monotonic manner with increase in gate-voltage ($-1\ \text{V} < V_g < 20$ V; regime IV). The hump-structure in the I-V_g data is unique for the modulation-doped sample and absent in SWNTs doped into *p*- or *n*-type along their entire lengths. The latter exhibit monotonic decrease or increase of conductance under increasing positive gate-voltages (*11–13, 15, 16, 18*).

The modulated chemical doping of the SWNT leads to an intratube *p*-*n* junction. Electron and hole concentrations at the two sides of the junction are further controlled by the gate. For regimes I, II, III, and IV in the I-V_g curve, the system can be assigned to p^+n, p^+n^+, pn^+, and nn^+, respectively (Fig. 2A). In regime I, a high negative gate shifts the conduction band and valence band up relative to the Fermi level, causing degenerate hole-doping to the left half of the tube (to p^+) and reduces electron density in the right half (to *n*). In this regime, the system shows certain rectifying I-V characteristics (Fig. 2B), resembling a leaking *p*-*n* junction accounted for theoretically in (*4*). In regime II, which displays the conductance hump, the increase in V_g from regime I enriches electrons in the right half of the tube, resulting in a p^+n^+ junction. The substantial conductance compared to the neighboring regimes and absence of rectification behavior (Fig. 2C) suggests that transport in this regime involves electron tunneling across the degenerately doped *p*-*n* junction. The depletion region is sufficiently thin for tunneling to occur, as shown below.

For the degenerately doped *p*-*n* junction in regime II, negative differential conductance (NDC) is observed at $T \leq 180$ K (Fig. 3A). The I-V curve recorded at 180 K exhibits NDC with a peak at $V = 0.12$ V and a valley at 0.16 V. NDC becomes more pronounced at lower temperatures, and a peak-to-valley ratio of ~1.5 is observed at 10 K. The appearance of NDC is consistent with the Esaki diode mechanism operating in heavily doped *p*-*n* junctions (*2*). Electrons tunnel between the conduction band of the *n* region and the valence band of the *p* region across a thin depletion region. This is responsible for the substantial conductance under reverse bias and low forward bias (Fig. 3, B and C). Beyond a certain point, increases in forward bias lead to decreases in current due to the conduction band of the *n*-side moving into the band gap of the *p*-side. The current decreases because there is no available state at the *p*-side for electrons tunneling into (Fig. 3D). Further increase in forward bias lowers the potential barriers for electrons and holes and the normal conduction mechanism of a forwardly biased *p*-*n* junction operates (*19*). This leads to the increase in current (Fig. 3D). NDC only appears around

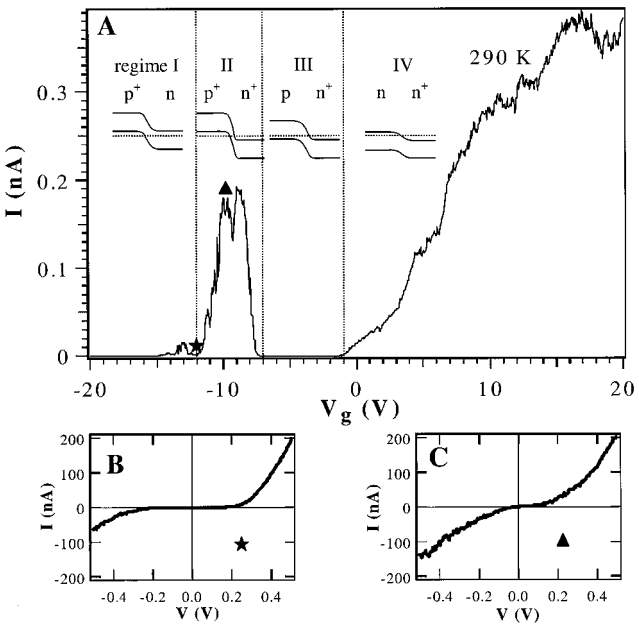

Fig. 2. Electrical properties of the modulation-doped SWNT at room temperature. (**A**) Current versus gate-voltage I-V_g curve recorded under a bias-voltage $V = 1$ mV. The drawings show the band diagrams in four regimes. (**B**) and (**C**) I-V curves recorded in regime I and II. The star and triangle in (A) mark the gate voltages for the I-V curves in (B) and (C), respectively.

$V = 0.16$ V and is consistent with the fact that NDC for an Esaki diode only appears at forward bias (*2*). NDC is not observed in other gate voltage regimes at temperatures >10 K, since the system does not consist of a p^+n^+ junction in these regimes.

The degree of electron and hole doping of the system and the depletion width can be estimated. The top of the conductance hump in regime II is at $V_g^* = -9.5$ V (Fig. 2A), where the two sides of the junction are degenerately doped with electrons and holes, respectively. For $V_g < V_g^a \sim -12$ V, electrons are depleted in the right half of the tube, and the system exhibits diminished conductance, whereas for $V_g \sim V_g^b \sim -7$ V, holes are depleted from the left half of the tube (Fig. 2A). Therefore, at the peak of the conductance hump where $V_g = -9.5$ V, the electron and hole densities are approximately $n_e \sim n_h \sim C_g(V_g^* - V_g^a) \sim C_g(V_g^b - V_g^*) \sim 62.5/\mu$m in the *n*- and *p*-sides, respectively. The unit length gate coupling capacitance $C_g = 4$ aF/μm is estimated from Coulomb charging data obtained at 4 K (Fig. 4A). The estimated charge densities correspond to ~0.6 electron and holes per 1000 carbon atoms for the *n*- and *p*-sides, respectively ($f = 0.6 \times 10^{-3}$). For similar doping degree f and a 1.5-nm SWNT ($E_g \sim 0.5$ eV) *p-n* junction, the depletion width is predicted to be $W \sim 10$ to 20 nm (*4*). The depletion width in our 2-nm nanotube *p-n* system should be on the order of several nanometers, because of the smaller energy gap ($E_g \sim 0.35$ eV) than the 1.5-nm tube considered by theory (*4*).

Regime IV (Fig. 2A) exhibits *n*-type semiconducting characteristics without NDC behavior at room temperature. At low temperatures, Coulomb blockade (CB) (*20–22*) accompanied by NDC with peak-to-valley ratio up to 3:1 show up in this regime (~4 K) (Fig. 4). The NDC characteristics differ from those seen in regime II at high temperatures (≥10 K) (Fig. 3A). They appear at both bias polarities, and multiple peaks exist on some of the *I-V* curves (Fig. 4A). Small changes in gate-voltage lead to substantial changes in the NDC structures. Also, the NDC appears at low bias-voltages (<50 mV), as opposed to ~0.16 V in the Esaki diode regime. A small energy scale is therefore involved in the NDC in regime IV.

Analysis of the CB data can shed some light into the origin of NDC in regime IV described above. The maximum Coulomb gap observed with the sample is ~80 mV in the *I-V* curves (Fig. 4A). We first treat the system as if it is dominated by a single quantum dot, because the conductance versus bias and gate-voltage plot (Fig. 4A, inset) shows nearly regular diamond structures (*20*). We obtain $U + \Delta E \sim 40$ meV for the quantum dot, where U is the charging energy and ΔE is the corresponding discrete energy level spacing. Both U and ΔE are inversely proportional to the length of the nanotube dot (*21–23*) with a typical ratio of $U/\Delta E \sim 6$ (*23*). This yields $U \sim 34$ meV and $\Delta E \sim 6$ meV. These energies correspond to a tube segment (dot) with length of ~100 to 150 nm (*21–23*), much smaller than the geometrical length of the SWNT (~3.5 μm) in the sample. The formation of a small dot on a long nanotube can occur from an inhomogeneous doping profile along the nanotube, a phenomenon that has also been observed with semiconducting SWNTs doped with potassium along their entire lengths (*16*). Fluctuations in the dopant concentration along the carbon nanotube lead to local band bending that can act as energy barriers in the tube (*16, 24, 25*). A small quantum dot can be formed when two such barriers separate a tube segment (~100 to 150 nm long) from the rest of the system. NDC can arise as a result of resonance tunneling through the discrete energy levels ($\Delta E \sim 6$ meV $> K_BT$ at 4 K) of the dot connected to *n*-type semiconducting source and drain. The valley of the NDC corresponds to an energy level in the dot falling below the conduction band of the source

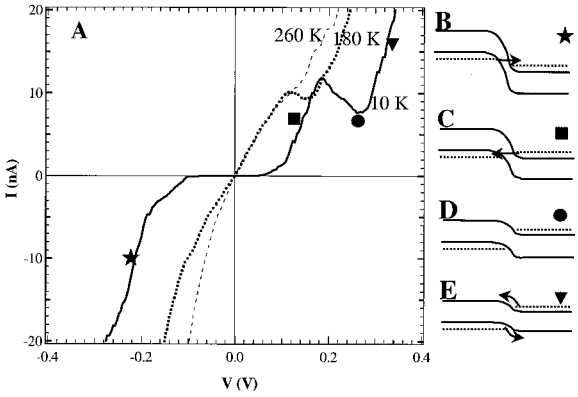

Fig. 3. Negative differential conductance in an intra-SWNT Esaki diode. (**A**) Current versus voltage *I-V* curves for regime II recorded at $V_g = -9.5$ V (p^+n^+ junction) at temperatures indicated. (**B** through **E**) Band diagrams show the transport mechanisms. The symbols in (B) through (E) match the ones in (A) labeling certain voltages. (B) through (E) illustrate the respective transport mechanisms under these voltages. At 10 K, the conductance of the system is suppressed near $V = 0$, and the NDC peak is shifted toward higher bias than that at 180 K. These two features could be related to the two metal-tube junctions in series with the intratube junction. For doped semiconducting SWNTs in general, band-bending effects at the metal-tube junctions typically leads to *I-V* curves with suppressed zero-bias conductance at low temperatures (*13*). Similarly, in the current system, the increased serial resistance at the metal-tube junctions at low temperatures causes the shift of the NDC peak to higher bias as well as the suppressed conductance region in *I-V*.

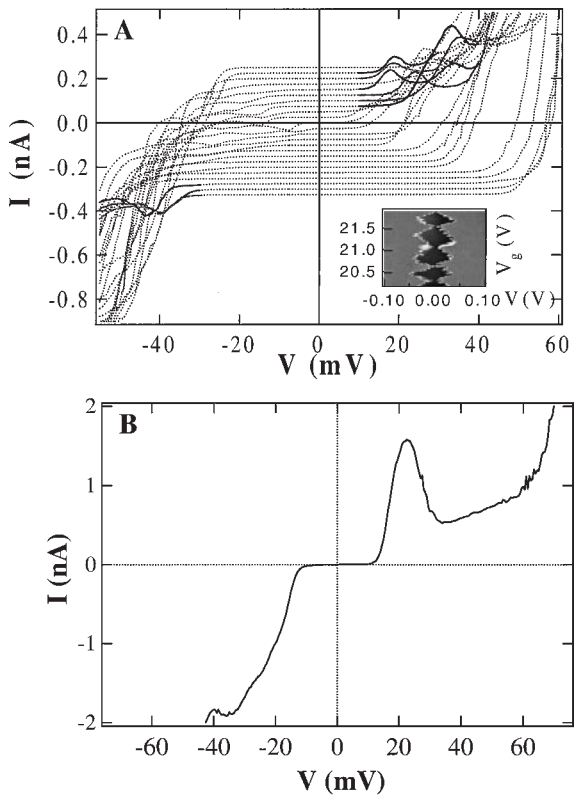

Fig. 4. Negative differential conductance and single-electron charging. (**A**) Current versus voltage *I-V* traces (dotted lines) recorded at 4 K in regime IV of Fig. 2A. The *I-V* curves are shifted along the current axis by 25 pA, and the increment in V_g between adjacent *I-V* curves is 10 mV. Certain regions of the *I-V* curves are shown in solid lines to highlight the NDC features. (Inset) Gray-scale two-dimensional plot of I versus V and V_g. Dark and bright areas represent low and high absolute-current regions, respectively. The Coulomb oscillations exhibit a period of $\Delta V_g \sim 0.4$ V, suggesting a gate capacitance of $e/\Delta V_g \sim 0.4$ aF coupled to the $L \sim 100$ nm tube-dot. A gate capacitance per unit length $C_g \sim 4$ aF/μm is estimated. (**B**) An *I-V* curve recorded at $V_g = 23.4$ V shows a pronounced NDC peak.

when the bias increases and no state is available for tunneling. This mechanism for negative differential conductance is similar to that in a double-barrier resonance tunnel diode (*26*).

The CB data (Fig. 4A) does show slight deviation from the characteristics of a perfect single-dot with incomplete Coulomb gap closure. Therefore, we cannot entirely rule out the possibility of dots in series on the nanotube (*27, 28*). A likely mechanism for NDC in this case is resonance tunneling through multiple discrete energy levels in adjacent dots. Two energy levels of double-dots involved in resonance tunneling and NDC have been observed in two-dimensional electron gas systems (*29*).

The high-temperature electrical characteristics of the sample shown here represent the results obtained with three modulation-doped SWNTs (diameters of ~2 nm). The modulated doping scheme reliably leads to intramolecular p^+n^+ junctions exhibiting negative differential conductance. At low temperatures, CB phenomena are consistently observed with the samples, but with the manifestation of unintentional doping modulation effects (not noticeable at high temperatures). This points to a need for much better control of the chemical homogeneity along the nanotube length. Most important, it also suggests that controlled doping modulations over a length scale of <100 nm along a nanotube should lead to well-defined quantum systems including coupled quantum dots. Modulated chemical doping of nanotubes holds promise as a new route to intramolecular devices.

References and Notes

1. W. Shockley, *IEEE Trans. Electron. Devices* **ED-23**, 597 (1976).
2. L. Esaki, *IEEE Trans. Electron. Devices* **ED-23**, 644 (1976).
3. C. Dekker, *Phys. Today* **52**, 22 (May 1999).
4. F. Leonard, J. Tersoff, *Phys. Rev. Lett.* **83**, 5174 (1999).
5. K. Esfarjani, A. A. Farajian, Y. Hashi, Y. Kawazoe, *Appl. Phys. Lett.* **74**, 79 (1999).
6. R. D. Antonov, A. T. Johnson, *Phys. Rev. Lett.* **83**, 3274 (1999).
7. L. Chico, V. H. Crespi, L. X. Benedict, S. G. Louie, M. L. Cohen, *Phys. Rev. Lett.* **76**, 971 (1996).
8. J. Hu, M. Ouyang, P. Yang, C. M. Lieber, *Nature* **399**, 48 (1999).
9. Z. Yao, H. W. C. Postma, L. Balents, C. Dekker, *Nature* **402**, 273 (1999).
10. J. Kong, H. Soh, A. Cassell, C. F. Quate, H. Dai, *Nature* **395**, 878 (1998).
11. S. Tans, A. Verschueren, C. Dekker, *Nature* **393**, 49 (1998).
12. R. Martel, T. Schmidt, H. R. Shea, T. Hertel, P. Avouris, *Appl. Phys. Lett.* **73**, 2447 (1998).
13. C. Zhou, J. Kong, H. Dai, *Appl. Phys. Lett.* **76**, 1597 (1999).
14. P. G. Collins, K. Bradley, M. Ishigami, A. Zettl, *Science* **287**, 1801 (2000).
15. J. Kong *et al.*, *Science* **287**, 622 (2000).
16. J. Kong, C. Zhou, E. Yenilmez, H. Dai, *Appl. Phys. Lett.*, in press.
17. R. S. Lee *et al.*, *Phys. Rev. B* **61**, 4526 (2000).
18. M. Bockrath *et al.*, *Phys. Rev. B* **61**, R10606 (2000).
19. B. G. Streetman, *Solid State Electronic Devices* (Prentice-Hall, Englewood Cliffs, NJ, 1995).
20. H. Grabert, M. H. Devoret, Eds., *Single Charge Tunneling* (Plenum, New York, 1992).
21. S. J. Tans *et al.*, *Nature* **386**, 474 (1997).
22. M. Bockrath *et al.*, *Science* **275**, 1922 (1997).
23. J. Nygard, D. H. Cobden, M. Bockrath, P. L. McEuen, P. E. Lindelof, *Appl. Phys. A* **69**, 297 (1999).
24. A. Bachtold *et al.*, *Phys. Rev. Lett.* **84**, 6082 (2000).
25. S. Tans, C. Dekker, *Nature* **404**, 834 (2000).
26. L. L. Chang, L. Esaki, R. Tsu, *Appl. Phys. Lett.* **24**, 593 (1974).
27. A. Bezryadin, A. Verschueren, S. Tans, C. Dekker, *Phys. Rev. Lett.* **80**, 4036 (1998).
28. P. L. McEuen, M. Bockrath, D. H. Cobden, Y.-G. Yoon, S. G. Louie, *Phys. Rev. Lett.* **83**, 5098 (1999).
29. N. C. vander Vaart, S. F. Godijn, Y. V. Nazarov, C. J. P. M. Harmans, J. E. Mooji, *Phys. Rev. Lett.* **74**, 4702 (1995).

30. Supported by the National Science Foundation, Defense Advanced Research Projects Agency/Office of Naval Research, Semiconductor Research Corporation/Motorola, a David and Lucile Packard Fellowship, a Terman Fellowship, the Laboratory for Advanced Materials at Stanford, National Nanofabrication Users Network at Stanford, the Camile Henry-Dreyfus Foundation, and the American Chemical Society.

15 August 2000; accepted 12 October 2000

Powering an Inorganic Nanodevice with a Biomolecular Motor

Ricky K. Soong,[1,2] George D. Bachand,[1,2] Hercules P. Neves,[1,2] Anatoli G. Olkhovets,[1,3] Harold G. Craighead,[1,3] Carlo D. Montemagno[1,2]*

Biomolecular motors such as F_1–adenosine triphosphate synthase (F_1-ATPase) and myosin are similar in size, and they generate forces compatible with currently producible nanoengineered structures. We have engineered individual biomolecular motors and nanoscale inorganic systems, and we describe their integration in a hybrid nanomechanical device powered by a biomolecular motor. The device consisted of three components: an engineered substrate, an F_1-ATPase biomolecular motor, and fabricated nanopropellers. Rotation of the nanopropeller was initiated with 2 mM adenosine triphosphate and inhibited by sodium azide.

Emergent fabrication techniques permit the construction of structures with features smaller than 7 nm (*1–4*). However, the construction of functional nanoelectromechanical systems (NEMS) is hindered by the inability to provide locomotive forces to power NEMS devices. The use of biomolecular motors such as enzymes offers an interesting alternative to silicon-based systems (*5, 6*). A number of enzymes such as kinesin (*7, 8*), RNA polymerase (*9*), myosin (*10*), and adenosine triphosphate (ATP) synthase (*5, 6, 11, 12*) function as nanoscale linear or rotary biological motors. The integration of biomolecular motors with nanoscale engineered systems enables the development of hybrid organic-inorganic devices capable of using ATP as an energy source. This approach may enable the creation of a new class of sensors, mechanical force transducers, and actuators.

The F_1-ATPase enzyme, which hydrolyzes ATP in living systems, is an excellent candidate for integration with NEMS for construction of rotary biomolecular motor–powered nanodevices (*5, 6*). The F_1-ATPase molecule, ~8 nm in diameter and 14 nm in length, is capable of producing ~80 to 100 pN·nm of rotary torque (*11, 12*). These characteristics of F_1-ATPase are compatible with the sizes and force constants of currently producible nanomechanical structures (*5, 6*). In addition, genetic modification of the F_1-ATPase sequence and structure has been used to precisely position individual F_1-ATPase molecules on engineered nanofabricated substrates (*13*). Previous studies have shown that actin filaments (5 nm in diameter and 1 to 4 μm in length) can be attached to the motor using biochemical techniques, and the resulting rotary motion can be visualized (*11, 12*). The integration of F_1-ATPase motors and nanofabricated mechanical systems, however, presents considerable engineering challenges with regard to the organic and inorganic interface (e.g., attachment chemistries, adhesion forces, and materials compatibility).

Our biomolecular motor–powered NEMS device consisted of three primary elements: (i) engineered, nanofabricated substrates of nickel (Ni) posts; (ii) recombinant F_1-ATPase biomolecular motors specifically engineered to selectively interface with nanofabricated structures; and (iii) engineered nanopropellers (Fig. 1). These elements were integrated into a functional unit using sequential attachment chemistries. Recombinant F_1-ATPase biomolecular motors were biotinylated immediately after purification and were then attached to the Ni posts using 10× histidine

[1]Nanobiotechnology Center, [2]Department of Agricultural and Biological Engineering, [3]School of Applied and Engineering Physics, Cornell University, Ithaca, NY 14853, USA.

*To whom correspondence should be addressed. E-mail: cdm11@cornell.edu